Constant-stress molecular dynamics: The phase diagram of silver iodide

J. L. Tallon
Physics and Engineering Laboratory, Department of Scientific and Industrial Research, Private Bag, Lower Hutt, New Zealand
(Received 25 March 1988)

The method of constant-stress molecular dynamics using the Parrinello-Rahman Lagrangian is described, particularly as applied to Coulomb systems. The method is used to simulate the phase behavior of silver iodide. The β, α, rocksalt, and liquid phases are reproduced and the boundaries are similar to those observed for real AgI. Evidence is found for the order-disorder transition in the α phase proposed by Perrott and Fletcher. This is characterized by a heat-capacity anomaly and a rise in the cation diffusion coefficient. The supercooled α phase and the equilibrium rocksalt phase both have diffuse fast-ion transitions and the latter cuts the rocksalt–α-phase boundary, causing it to cusp in to an apparent triple point with the α-phase order-disorder transition.

I. INTRODUCTION

The phase behavior of cyrstalline silver iodide is rich in variety. In the single material one finds under ambient conditions, a mixed $\beta+\gamma$ phase (wurzite and zinc blende), while at elevated pressure a rocksalt phase becomes stable and at elevated temperature there occurs the α phase (bcc) which is a fast-ion conductor, i.e., the anion sublattice remains localized while the cation sublattice is diffusive. Below room temperature the $\beta+\gamma$ and rocksalt phases become separated by an intermediate phase to which transitions from either side are very sluggish. The phase diagram, as determined by Mellander, Bowling, and Baranowski,[1] and Akella, Vaidya, and Kennedy,[2] is shown in Fig. 1. In the past ten years much attention has been focused on the α phase as an archetypical fast-ion conductor of the kind where additional sites are available to the highly mobile species, in this case the cations. There are no less than six equivalent tetrahedral sites available to each cation. Recently[3,4] it has been found that the rocksalt phase has a diffuse transition to fast-ion behavior, the location of which is shown by the dashed line in the figure. Here, there are no additional sites so that site hopping is only achieved either by site sharing or by correlated hopping in closed loops as in fluorites.[5] One therefore finds, in a single system, archetypes for the two modes of fast-ion conduction.

Complex as this phase diagram may be, two additional features have been proposed that may further enrich the behavior. Perrott and Fletcher[6] have proposed that an order-disorder transition takes place in the α phase driven by distribution of the cations over the equivalent tetrahedral sites as well as possibly trigonal and then octahedral sites. In strictly stoichiometric samples they observed a λ-like heat capacity at 430 °C, indicating a transition that ran away to first order. Small departures from stoichiometry, however, were sufficient to suppress the effect. Subsequent investigations have proved inconclusive and even contradictory. Jost[7] and Allen and Lazarus[8] found no anomaly in the ionic conductivity of α-AgI in the vicinity of 430 °C, while Jansson and Sjöblom[9] found a λ-like behavior in the thermal expansion there, though rather smaller than one would expect from the heat-capacity data. They also subsequently found changes in rheological properties there,[10] as did Mariotto *et al.*[11] for the Raman depolarization ratio. More recently, Mellander[3] found no heat-capacity anomaly using differential scanning calorimetry even if the AgI were precipitated in the same manner as used by Perrott and Fletcher.[6] The order-disorder transition therefore remains to be confirmed. Lattice-gas calculations on the tetrahedral sites under a mean-field approximation by Szabó[12] indicate that the disordering is inevitable provided melting does not occur first, and moreover two further intermediate states are possible.

The second possible extension of the phase diagram which interests us here concerns the path taken by the α-phase–rocksalt boundary as it completes its course to the crystal-liquid triple point. Tallon and Buckley[4] de-

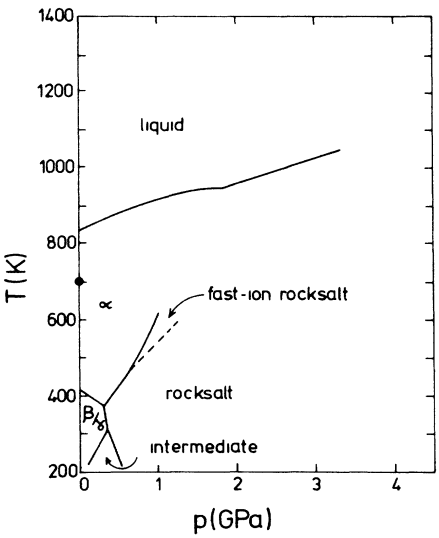

FIG. 1. The phase diagram of AgI as determined by Mellander *et al.* (Ref. 1) and Akella *et al.* (Ref. 2). The dashed line indicates the diffuse fast-ion transition in the rocksalt phase and the solid data point indicates the order-disorder transition inferred by Perrott and Fletcher (Ref. 6).

duced from transition entropy data that this boundary must curve more steeply upward as a consequence of the fast-ion transition in the rocksalt phase, the slope possibly even changing sign. To enable the boundary to then swing out again towards the known triple point, the α phase must exhibit an anomalous rise in entropy which they proposed derived from the order-disorder transition. Indeed, because the location of phase boundaries is determined by a rather fine balance between state free energies, the shape of this boundary must be a very sensitive test for the existence of the α-phase order-disorder transition.

In the present work we report the results of a molecular dynamics (MD) simulation of AgI in which the entire phase diagram is mapped and particularly the shape of the rocksalt–α-phase boundary. Exploratory work on the β-α transition at zero pressure has already been presented by Parrinello, Rahman, and Vashishta[13] (PRV). Our goal has not been to develop a set of potentials which closely reproduce the phase behavior of AgI. Rather, we have adopted the simple rigid-ion potentials of PRV to explore the above ideas in the knowledge that they at least lead to stable α and β phases. We find a stable rocksalt phase possessing a diffuse fast-ion transition which indeed distorts the α-phase–rocksalt boundary. Moreover, a subsequent fall in slope of this boundary prior to the crystal-liquid triple point suggests that the α phase of our model system does undergo a disordering transition. This is confirmed by a hump in the heat capacity and enhanced fluctuations in the α phase at zero external pressure. A brief account of this work has already been presented.[14]

One cannot effectively study these transitions with conventional microcanonical MD computations as the constant volume constraint precludes the attendant changes in box size and shape. The shear stresses arising from isochoric transitions would rise to prohibitive levels. The first step towards dealing with this kind of problem was made by Andersen[15] who performed isobaric calculations by allowing the volume to vary as an additional dynamical variable. Parrinello and Rahman[16] extended this by allowing the nine dynamical variables describing both size and shape of the MD cell to fluctuate so as to maintain constant stress. They adopted a generalized set of $3N+9$ model Langrangian equations of motion which allow a strict conservation of a generalized enthalpy. Contrary, however, to conventional MD where volume is strictly conserved, these are constant-stress calculations only in the sense that the stress fluctuates about some prescribed value. It was this method which was employed by PRV to demonstrate the α-β transition in AgI. However, as the details of the technique, particularly as applied to Coulomb systems, were sketchy, we first devote some space to these. Following that, we report the results obtained by applying this technique to the PRV model–AgI system.

II. EQUATIONS

A. Parrinello-Rahman Lagrangian

Consider an assembly of N particles [with masses m_i, $i=1,\ldots,N$, and pair interaction potential $\phi(r)$] moving in an arbitrary parallelepiped MD cell. The edges of the box are the vectors $\mathbf{b}_1$, $\mathbf{b}_2$, and $\mathbf{b}_3$ which need be neither equal in magnitude nor mutually orthogonal. The box is conveniently described as the matrix $\underline{B}=\{\mathbf{b}_1,\mathbf{b}_2,\mathbf{b}_3\}$ and the box volume is the determinant of this matrix $\Omega=\det\underline{B}$. The positions of the particles within the central MD box are defined by a set of (soft) internal relative vectors $\mathbf{s}_i$, with $-\frac{1}{2}\le s_{i1},s_{i2},s_{i3}<\frac{1}{2}$, such that the absolute (hard) position vectors $\mathbf{r}_i$ are given by the transformation

$$\mathbf{r}_i=\underline{B}\mathbf{s}_i \ . \tag{1}$$

Clearly the relative separation, r_{ij} of particles i and j is obtained from

$$r_{ij}^2=(\mathbf{s}_i-\mathbf{s}_j)'\underline{M}(\mathbf{s}_i-\mathbf{s}_j) \ , \tag{2}$$

where the prime denotes the transpose of a vector or matrix and $\underline{M}=\underline{B}'\underline{B}$ is the metric of the transformation.

The Lagrangian introduced by Parrinello and Rahman[16] is as follows:

$$\mathcal{L}=\tfrac{1}{2}\sum_i m_i\dot{\mathbf{s}}_i'\underline{M}\dot{\mathbf{s}}_i-\sum_i\sum_{j\,(>i)}\phi(r_{ij})+\tfrac{1}{2}\mu\mathrm{Tr}(\dot{\underline{B}}'\dot{\underline{B}})-p\Omega \ . \tag{3}$$

Here, the overdot denotes time derivatives, p is the external pressure, and μ, which has units of mass, arises from the kinetic term associated with the fluctuation in $\underline{B}$. The value of μ determines the time scale, only, of these fluctuations and not the structure of the particles enclosed. Its arbitrariness therefore allows one to match the time scales of box and particle fluctuations. It is important to stress that the momentum of the particle is defined as $m_i\underline{B}\dot{\mathbf{s}}_i$ and not $m_i(\dot{\underline{B}}\mathbf{s}_i+\underline{B}\dot{\mathbf{s}}_i)$.

This Lagrangian is to be understood in a formal sense as being a convenient means of allowing the particles and box walls to dynamically interact. As such, since there is no symmetry constraint on $\underline{B}$, there are $3N+9$ degrees of freedom in the system and these evolve according to the following Lagrangian equations of motion:

$$\ddot{\mathbf{s}}_i=m_i^{-1}\sum_{j\,(\neq i)}\chi(r_{ij})(\mathbf{s}_i-\mathbf{s}_j)-\underline{M}^{-1}\dot{\underline{M}}\dot{\mathbf{s}}_i, \quad i,j=1,\ldots,N$$

and (4)

$$\ddot{\underline{B}}=\mu^{-1}(\Pi-p\underline{I})\underline{\sigma} \ .$$

Here, $\chi(r)=-r^{-1}d\phi/dr$; $\underline{I}$ is the identity matrix; the matrix $\underline{\sigma}=\{\mathbf{b}_2\times\mathbf{b}_3,\mathbf{b}_3\times\mathbf{b}_1,\mathbf{b}_1\times\mathbf{b}_2\}$ describes the faces of the MD cell; and $\underline{\Pi}$, the internal stress tensor, is the dyadic generalization of the virial pressure,

$$\Omega\Pi=\sum_i m_i\mathbf{v}_i\cdot\mathbf{v}_i+\sum_i\sum_{j\,(>i)}\chi(r_{ij})(\mathbf{r}_i-\mathbf{r}_j)\cdot(\mathbf{r}_i-\mathbf{r}_j) \ . \tag{5}$$

Following Parrinello,[17] we prescribe μ by equating the transit time of a longitudinal wave with the period of isotropic oscillation of the box with the result

$$\mu=(3/4\pi^2)\sum_i m_i \ . \tag{6}$$

As observed by Parrinello,[17] the Lagrangian $\mathcal{L}$ conserves a generalized enthalpy $\mathcal{H}$ given by

$$\mathcal{H}=E_k+E_p+p\Omega+\tfrac{1}{2}\mu\,\mathrm{Tr}\{\dot{\underline{B}}'\dot{\underline{B}}\}$$
$$=H+\tfrac{1}{2}\mu\mathrm{Tr}\{\dot{\underline{B}}'\dot{\underline{B}}\}\ , \tag{7}$$

which with the exception of the last term coincides with the usual enthalpy, H of the assembly. E_k and E_p are the kinetic and potential energies of the particles. The last term in $\mathcal{H}$ is the box kinetic energy which at equilibrium is $\frac{9}{2}k_BT$, where k_B is Boltzmann's constant and T is the absolute temperature. In contrast, $E_k=\frac{3}{2}Nk_BT$ so to order $(3/N)$ the system is an isenthalpic, isobaric ensemble.

B. Verlet algorithm

In the common Verlet[18] algorithm for stepwise integration of the equations of motion the current unbalanced force on a particle is determined by the current positions only. From this force, new positions at a discrete time step later are calculated and the current velocity is given by the displacement from the old to the new position, ignoring the current position. Now with a fluctuating box, the current forces are determined by current positions and *velocities* as shown by Eq. (4). The simple Verlet process must therefore be rearranged to obtain closure of the recursion scheme in the form

$$\{\underline{I}+\tfrac{1}{2}\Delta t\underline{M}^{-1}\dot{\underline{M}}\}\mathbf{s}_i(t+\Delta t)=2\mathbf{s}_i(t)-\{\underline{I}-\tfrac{1}{2}\Delta t\underline{M}^{-1}\dot{\underline{M}}\}\mathbf{s}_i(t-\Delta t)+\Delta t^2m_i^{-1}\sum_{j\,(\neq i)}\chi(r_{ij})[\mathbf{s}_i(t)-\mathbf{s}_j(t)]\ , \tag{8}$$

where Δt is the discrete time step. Apart from the factors in curly brackets this expression is identical to the Verlet algorithm. In general, these factors are not small perturbations to the identity matrix so the matrix factor on the left-hand side must be inverted.

Periodic boundaries are incorporated in the usual way by, for each i, adding or subtracting the value 1 from a new soft coordinate s_{i1}, s_{i2}, or s_{i3} should that coordinate exceed the range $[-\frac{1}{2},+\frac{1}{2}]$. The same must then be done for the corresponding current soft coordinate. Specifically, for each iteration $\mathbf{s}_i(t+\Delta t)$ is replaced by $\mathbf{s}_i(t+\Delta t)-\mathbf{U}$ and $\mathbf{s}_i(t)$ by $\mathbf{s}_i(t)-\mathbf{U}$, where $\mathbf{U}$ is the integral component of $2\mathbf{s}_i(t+\Delta t)$.

With a fluctuating box, boundary traversal necessitates great care in the evaluation of mean-square displacements. In conventional MD simulation these are often calculated by generating the following sequence of particle positions:

$$\mathbf{S}_{i,n+1}=\mathbf{S}_{i,n}+\mathbf{s}_i(t+\Delta t)-\mathbf{s}_i(t)\ . \tag{9}$$

The cancellation of the $\mathbf{U}$'s on the right-hand side yields the soft piecewise linear path $\mathbf{S}_{i,n}$ for each original particle diverging throughout the quasi-infinite system, whereas the $\mathbf{s}_i$ gives the paths of each successive image particle after it enters, and only while it remains in, the central MD cell. If the box size and shape is allowed to evolve, one must be careful to use the same prescription and then transform to the absolute position $\mathbf{R}_{i,n}=\underline{B}(t)\mathbf{S}_{i,n}$ rather than following the temptation to construct directly,

$$\mathbf{R}_{i,n+1}=\mathbf{R}_{i,n}+\underline{B}(t+\Delta t)\mathbf{s}_i(t+\Delta t)-\underline{B}(t)\mathbf{s}_i(t)\ , \tag{10}$$

which introduces an arbitrary deviation each time a boundary is traversed.

C. Coulombic systems

The equations in Sec. II A are generally valid whatever the pair interaction, but in practice concerns of computational thrift require that the potential be truncated and, for conventional MD usually at a maximum of $\frac{1}{2}$ the box length. This gives no problem with the short-range potentials but for long-range Coulombic interactions it necessitates use of the well-known Ewald summation technique.[19,20] Even in the case of short-range potentials, introduction of fluctuations in the MD cell requires a recurring redefinition of cutoff lengths while, for the Coulomb interaction, both computational strategy and basic equations must be altered.

The Ewald method as applied to conventional MD calculations, is reviewed in detail by Rahman and Vashishta.[20] It may be understood as formally enveloping each point charge by a spherical charge of opposite sign so that the local potential falls off sufficiently rapidly with distance. The total forces and energy from such a system can be evaluated as a short-range interaction along with the other short-range potentials and need not concern us here except to note that this real-space part of the Coulomb force has a convergence factor $\exp(-\alpha^2r_{lj}^2)$. The additional energy of the assembly of spherical charge distributions is evaluated in reciprocal space to be

$$\Phi_{\mathrm{rec}}=(2\pi/\Omega)\sum_{\mathbf{G}}{}'\,|s(\mathbf{G})|^2G^{-2}\exp(-G^2/4\alpha^2)\ , \tag{11}$$

where the reciprocal-lattice vectors $\mathbf{G}$ span an integral mesh of reciprocal-lattice vectors excluding, as indicated by the prime on the summation, $\mathbf{G}=\mathbf{0}$. The $S(\mathbf{G})$ are the structure factors

$$S(\mathbf{G})=\sum_j q_j\exp(i\mathbf{G}\cdot\mathbf{r}_j)\ , \tag{12}$$

and α, the convergence constant, is effectively determined by the radius of the charge distribution. It is chosen so as to balance the efficiency of the real and reciprocal space summations.

The force on a particle, l arising from the reciprocal-space part of the energy is

$$-\partial\Phi_{\mathrm{rec}}/\partial\mathbf{r}_l$$
$$=-(2\pi/\Omega)\sum_{\mathbf{G}}{}'\left[i\mathbf{G}q_le^{i\mathbf{G}\cdot\mathbf{r}_l}\sum_j q_je^{-i\mathbf{G}\cdot\mathbf{r}_j}+\mathrm{c.c.}\right]$$
$$\times G^{-2}\exp(-G^2/4\alpha^2)\ . \tag{13}$$

The mesh of reciprocal-space vectors $\mathbf{G}$ is a linear integral combination of the reciprocal-lattice vectors $2\pi\mathbf{b}_2\times\mathbf{b}_3/\det\underline{B}$, etc. which are orthogonal to the box edges, viz.,

$$\mathbf{G}=2\pi\underline{B}'^{-1}\mathbf{K},\ \mathbf{K}=(k,l,m),\quad k,l,m=0,1,2,\ldots . \tag{14}$$

This orthogonality ensures that the projection of reciprocal-space vectors on real-space vectors is the same irrespective of whether the vectors are hard or soft, i.e.,

$$\mathbf{G}\cdot\mathbf{r}\equiv\mathbf{K}\cdot\mathbf{s} .$$

The numerical construction of Eq. (14) is usefully simplified by this identity and the metric only enters in evaluating G^2,

$$G^2=4\pi^2\mathbf{K}'\underline{M}^{-1}\mathbf{K} . \tag{15}$$

The reciprocal-space contribution to the stress matrix $\Pi_{\rm rec}\partial\Phi_{\rm rec}/\partial\underline{\epsilon}$, where $\underline{\epsilon}$ is the strain matrix, may be evaluated from Eq. (12) by noting that for $\mathbf{G}\rightarrow\mathbf{G}-\delta\underline{\epsilon}\mathbf{G}$,

$$\delta G^2=2\mathbf{G}'\delta\underline{\epsilon}\mathbf{G} \tag{16}$$

so that

$$\underline{\Pi}_{\rm rec}=(2\pi/\Omega)\sum_{\mathbf{G}}{}'\,|S(\mathbf{G})|^2G^{-2}\{\underline{I}-2\mathbf{G}\cdot\mathbf{G}G^{-2}-\tfrac{1}{2}\mathbf{G}\cdot\mathbf{G}\alpha^{-2}\}\times\exp(-G^2/4\alpha^2) . \tag{17}$$

The first term arises from $\partial\Omega/\partial\underline{\epsilon}$ and is just the reciprocal-space part of the Coulomb energy.

The central practical aspect of the Ewald summation is to balance the convergence of the real-space and reciprocal-space energy and force sums through appropriate choice of the value of α. For small α the reciprocal-space summation is rapidly convergent, while for large α convergence is most rapid with the real-space sum. By selecting $\alpha\times$(box edge)~ 5.6, it is possible to restrict the real space sum to the first term only,[21] namely the minimum image interactions for pairs within the central MD cell only, thus excluding pairs separated by more than half the box length. This leaves a manageable number of terms arising from a reasonably small sphere of soft vectors $\mathbf{K}=(k,l,m)$. However, if we are to allow the box to fluctuate we need to develop some prescription for reviewing both the value of α and the cutoff radius for the sphere of vectors $\mathbf{K}$. This also has bearing on the evaluation of radial-distribution functions and on pressure and energy corrections arising from the finite cutoff. These features will now be discussed.

D. Truncation length

The appropriate real-space cutoff length R_c for pair correlations and interaction potential is the radius of the largest inscribed sphere in the central MD cell. As the normal separation between opposite faces is $\mathbf{b}_1\cdot\mathbf{b}_2\times\mathbf{b}_3/|\mathbf{b}_2\times\mathbf{b}_3|$, etc.,

$$R_c=\tfrac{1}{2}\det\underline{B}[\min(|\mathbf{b}_2\times\mathbf{b}_3|^{-1},|\mathbf{b}_3\times\mathbf{b}_1|^{-1},\times|\mathbf{b}_1\times\mathbf{b}_2|^{-1})] . \tag{18}$$

But for the factor π these are the inverses of the reciprocal-lattice vectors. In anticipation of our requirements below we let $R_{\rm max}$ be the maximum of these normal halfwidths, corresponding to the minimum of the reciprocal-lattice vectors.

Suppose we wish to evaluate real- and reciprocal-space contributions to the same accuracy A. The two convergence factors in those contributions then must satisfy

$$\exp(-\alpha^2R_c^2)=A=\exp(-G_c^2/4\alpha^2) . \tag{19}$$

The first of these equations determines α while the second determines the truncation radius, G_c for the sphere of G vectors, viz.,

$$G_c=-(2/R_c)\ln A . \tag{20}$$

Now, to find the maximum value of k, l, or m in Eq. (18) which must be spanned in order to obtain all the vectors $\mathbf{G}$ such that $G\le G_c$, we note that this occurs for vectors parallel to the shortest reciprocal-lattice vector. Thus, from Eqs. (14) and (20),

$$k_{\rm max}=-(2/\pi)\ln A(R_{\rm max}/R_c) . \tag{21}$$

In this way α, G_c, and $k_{\rm max}$ may be modified as R_c evolves during a simulation and these are, of course, determined by the current value of R_c. On the other hand, pair correlations may only be determined out to the smallest value of R_c encountered during an entire equilibration otherwise information is lost near the surface of the correlation sphere.

Finally, we must note that since the truncation radius R_c fluctuates and at times exhibits monotonic transient behavior, corrections to pressure and energy arising from ions beyond R_c will not be constant. For systems comprising less than 500 ions with dipole or van der Waals interactions, these corrections are rather significant and consequently the system will not follow an isenthalpic trajectory through configuration space unless truncation corrections are made to the stress tensor given by Eq. (5). We attempted to do this using the virial expression for the pressure, fixing the pair-distribution function $g_{\alpha\beta}(r)$ at the value 1 for all $r>R_c$, an approximation which is best at high temperature where the peaks in $g_{\alpha\beta}(r)$ are well broadened. These truncation corrections were included in the algorithm for updating the box matrix; however, the assumption of uniform density beyond the truncation radius rendered the assembly unstable at pressures below about 1 GPa. Instead, we simply noted the change in enthalpy during what should have been an isenthalpic transition and corrected measured enthalpies beyond the transition by subtracting the observed enthalpy change. The displacement of the transition point is calculable from this change.

III. MODEL AND METHOD

In studying phase transitions by molecular dynamics, one ideally requires a large system in order to diminish the effect of interfacial energies. However, as the intention was to map an extensive area of the phase diagram, it was necessary to adopt a compromise of 216 or 256

ions in the central assembly. The former number was appropriate for commencing calculations in the rocksalt phase with a cubic box, while the latter was used for starting in the α phase. This meant that the crystal-liquid boundary could be mapped along its length using an approximately cubic box. The smallness of the system size is a point of concern. This will not greatly affect equilibrated data points in a single phase state, but is likely to induce hysteresis at transition boundaries due to increased nucleation barriers.

As already noted, the interaction potential adopted is that due to PRV, namely

$$\begin{aligned}\phi_{\alpha\alpha}(r)&=H_{\alpha\alpha}r^{-n_{\alpha\alpha}}+0.36r^{-1}\ ,\\ \phi_{\alpha\beta}(r)&=H_{\alpha\beta}r^{-n_{\alpha\beta}}-0.36r^{-1}-1.1736r^{-4}\ ,\\ \phi_{\beta\beta}(r)&=H_{\beta\beta}r^{-n_{\beta\beta}}+0.36r^{-1}-2.3172r^{-4}\\ &\quad -6.9371r^{-6}\ ,\end{aligned} \tag{22}$$

where α refers to silver ions and β to iodine ions and $H_{\alpha\beta}=A(\sigma_\alpha+\sigma_\beta)n_{\alpha\beta}$. Length units are in angstroms and energy units are given by $\varepsilon^2/(\text{Å})=14.39$ eV where ε is the vacuum permittivity. σ_α ($=0.53$ Å) and σ_β ($=2.2$ Å) are the ionic radii and $n_{\alpha\alpha}=11$, $n_{\alpha\beta}=9$, and $n_{\beta\beta}=7$. The adequacy of the above interaction has already been borne out by the results of PRV and has been successfully applied to compare MD calculations with neutron inelastic scattering.[22] We note further that we found conventional MD calculations along the $V=33.25$ cm^3/mol isochore in the rocksalt phase yielded a constant slope $(\partial P/\partial T)_V=2.7\times10^6$ Pa/K. This quantity is identical to the product αB_T where α is the volume coefficient of thermal expansion and B_T is the isothermal bulk modulus. For real AgI the value of this quantity at the same volume is 2.8×10^6 Pa/K.[4]

Various methods may be employed to determine the location of phase boundaries. The central problem is that the nucleation barriers associated with first-order phase transitions, and the absence of nucleation sites in our idealized quasi-infinite assembly, make superheating and supercooling beyond phase boundaries inevitable. One can perform thermodynamic calculations provided that reversible thermodynamic paths between the two phases can be devised.[23] The present technique, however, offers a more direct and efficient means of locating both boundaries and transition parameters, provided that appropriate precautions are taken. Moreover, the kinetics and mechanism of the transitions may also be studied. Methods used are as follows.

(i) The Volmer-Weber-Becker-Döring theory of nucleation of phase change[24] has the transition rate proportional to the change in free energy times a Boltzmann factor (which incorporates the nucleation barrier). The change in free energy is proportional to the degree of superheating or supercooling whether temperature or pressure is the controlled parameter. Plotting the observed transition rate as a function of temperature or pressure allows one to extrapolate back to zero transition rate of obtain the thermodynamic equilibrium transition point. This method was used most successfully on the rocksalt-β–phase boundary where, as the boundary is nearly vertical and hence the enthalpy change is rather small, temperature increments on traversing the boundary are small.

(ii) These temperature increments on traversing a boundary may be used to estimate transition parameters. Two traverses are available: isobaric, where temperature is incremented at constant pressure, and adiabatic, where the prescribed pressure only is incremented. We consider the latter here and the former under (iii).

Consider the adiabatic traverse, illustrated in Fig. 2, from phase II to phase I across the phase boundary where the transition nucleates at (p_3,T_3) and proceeds at constant enthalpy terminating at (p_3,T_4). An adiabat is given by

$$(\partial p/\partial T)_s\equiv C_p/\alpha VT\ , \tag{23}$$

so that for infinitesimal increments

$$T_3-T_1=(\alpha VT/C_p)_{\rm II}(p_3-p_1) \tag{24}$$

and

$$T_4-T_0=(\alpha VT/C_p)_{\rm I}(p_3-p_0)\ , \tag{25}$$

where the subscript I or II refers to one or other of the two phases. The entropy change along the alternative path via (p_1,T_0) and (p_0,T_0) being an isobar, followed by an isoterm, an equilibrium phase transition followed by an adiabat, is

$$(C_p/T)_{\rm II}(T_0-T_1)-(\alpha V)_{\rm II}(p_0-p_1)+\Delta S_t=0\ . \tag{26}$$

Finally, as

$$(T_1-T_0)/(p_1-p_0)=dT_t/dp \tag{27}$$

one obtains

$$T_3-T_4=T_0\frac{\Delta S_t}{C_p^{\rm II}}+(T_4-T_0)\left[\frac{(C_p/\alpha V)_{\rm I}}{(C_p/\alpha V)_{\rm II}}-1\right]\ . \tag{28}$$

In the ideal case where $(p_3,T_4)\equiv(p_0,T_0)$, this reduces to

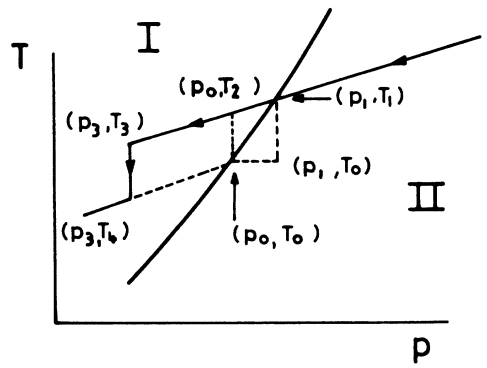

FIG. 2. Solid curve: adiabatic traverse of a phase boundary from phase II to phase I. Nucleation of the final phase commences at (p_3,T_3) and transformation proceeds at constant pressure and is complete at (p_3,T_4). The dashed alternative path is isobaric at p_1, isothermal at T_0, the transformation occurs at the phase boundary at (p_0,T_0) and finally, is adiabatic to (p_3,T_4).

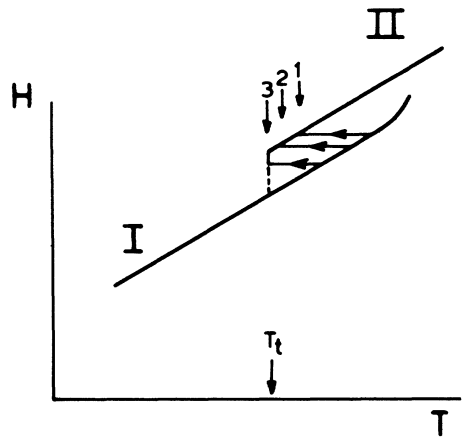

FIG. 3. Isobaric transition from phases I to II. At large superheating the system transforms at constant enthalpy to T_1 lying above the equilibrium transition point T_t. At lower superheating the transition rate diminishes and the final temperature after transition falls but no lower than T_t.

$$T_2 - T_0 = T_0 \Delta S_t / C_p^{\mathrm{II}} \ . \tag{29}$$

Thus, provided one knows the heat capacity of the initial phase, temperature increments following adiabatic traverses of a phase boundary give a direct measure of the transition entropy. Moreover, in the absence of heat-capacity data, C_p may be estimated from an adiabatic path in the initial phase.[4] In principle, the equilibrium transition temperature, T_0 may be located by method (i) above but in practice the nucleation barrier may be sufficiently large that the minimal adiabatic transition $T_2 \rightarrow T_0$ cannot be achieved. Even so, Eq. (28) may be used with sufficient accuracy to estimate ΔS_t by neglecting the second term on the right-hand side, which is a small correction.

(iii) The final and most straightforward method used to locate transition parameters was under isobaric conditions and is illustrated in Fig. 3. Phase I is superheated and transforms at constant enthalpy to phase II with final temperature T_1. The process is repeated with a smaller degree of superheating and as a consequence the nucleation and transformation time increases and the final temperatures T_2, T_3, etc. reduce until the limiting value T_t is reached. The fact that all of the transitions investigated proceeded with relatively little superheating, apparently well away from any spinodal instability, is probably due to the smallness of the system and the fact that not just local density, but total density was fluctuating.

IV. RESULTS

Across the entire equilibrium extent of the α phase we found our system to be fast-ion conducting. On supercooling beyond the β boundary, however, at (0 GPa, 300 K) or (1 GPa, 420 K) we found a diffuse fast-ion transition to a normal α phase where the silver ions remain localized in the tetrahedral positions. Unfortunately, it was not possible to follow the α phase all the way to the normal state as the substantial reduction in entropy of that phase at the diffuse transition provided a large thermodynamic potential driving the system to the β phase. Diffusion coefficients for the mobile silver ion were measured from the linear part of diverging mean-square displacements over periods of the order of 5 to 10 ps. These are plotted in Arrhenius form in Fig. 4 for pressures of 0, 1, and 2 GPa. The data can be consistently separated into two linear regions at low and high temperatures with effective activation enthalpies h_m of 0.087 ± 0.007 eV and 0.22 ± 0.02 eV, respectively. The low-temperature value is in excellent agreement with the value for real AgI,[3] $h_m = 0.098$ eV which is found to be independent of pressure. The fast-ion transitions to normal ionic behavior are indicated by the plunging arrows.

The fast-ion transition in the rocksalt phase was readily observable firstly as a Schottky hump in thermal expansion and heat capacity and more conclusively by the diffusion coefficient for the silver ions rising up above zero. This is shown in Fig. 5 for pressures of 2, 3, and 4 GPa. Radial-distribution functions (RDF's) determined for the system quenched from this region confirmed that the structure was still that of rocksalt. There was no indication that the quench resulted in a change in structure, and RDF's obtained in the fast-ion region showed an occupancy of 6 in the nearest unlike-neighbor shell and 12 in the nearest like-neighbor shell. There was, therefore, no suggestion of transition to the bcc structure for which these numbers are, respectively, 4 and 14. The complete phase diagram as determined in this work for the simulated AgI is given in Fig. 6 and the diffuse fast-ion transition line is shown by the dashed line in the rocksalt phase. This line is the locus of plateaux in temperature during constant heating rate runs.

Transition from a cube of rocksalt AgI to the ideal shape for 216 ions of β-AgI requires an orthorhombic distortion of $\sqrt{3}$ along one axis, and $2\sqrt{2/3}$ along another. Figure 7 shows B_{22}/B_{11} and B_{33}/B_{11} for the assembly

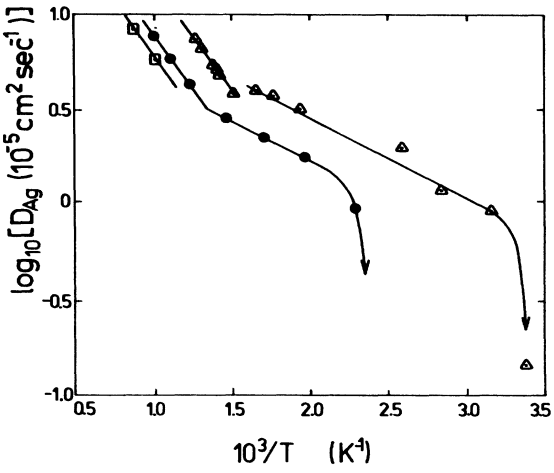

FIG. 4. Silver-ion diffusion coefficients for α-AgI determined from mean-square displacements. Triangles: pressure = 0 GPa. Circles: 1 GPa. Squares: 2 GPa. The downward arrows indicate diffuse fast-ion transitions occurring at (0 GPa, 300 K) and (1 GPa, 420 K).

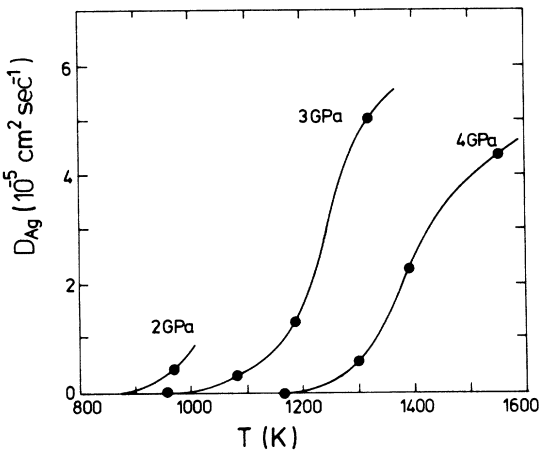

FIG. 5. Silver-ion diffusion coefficients for rocksalt-AgI showing a diffuse fast-ion transition along isobars of 2, 3, and 4 GPa.

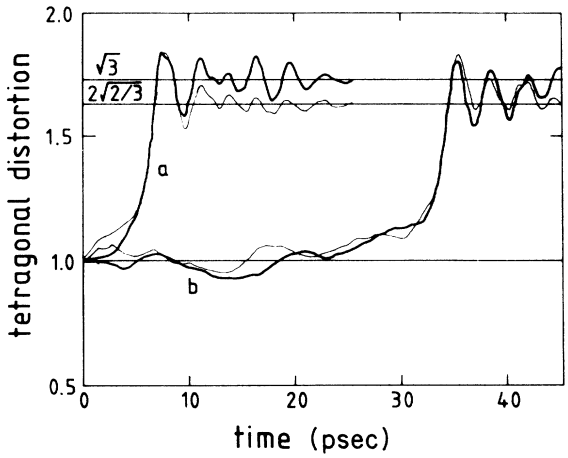

FIG. 7. The orthorhombic distortions B_{22}/B_{11} and B_{33}/B_{11} during transformation from rocksalt to β-AgI. (a) $P=0$ GPa, (b) $P=0.19$ GPa.

transforming at 359 K at pressures of 0 and 0.19 GPa. As discussed above, nucleation time depends on the proximity to the transition point (0.21 GPa), but, following nucleation, we found that the distortions progressed to their ideal values, and oscillations about these values gradually dissipated. RDF's for systems quenched from these final equilibrated states confirm the wurzite structure, but sometimes a small amount of zinc-blende structure was entrapped. Similarly, transitions from the rocksalt to the α phase displayed the ideal $\sqrt{2}$ tetragonal distortion as shown in Fig. 8 and again the final structure was confirmed by determining RDF's.

The open data points in Fig. 6 indicate equilibrium transition points determined in the main by method (iii) discussed in Sec. III. The solid curves are a reasonable connection of these data points based mainly on the geometrical constraints of smoothly joining the data, but guided also by transition slopes dT_t/dp determined below from transition increments in enthalpy and volume. The slope for the β to α transition is indeed negative as is the volume change across the transition. The dashed extension of the rocksalt to α transition rises to the data point in the liquid region which was determined for superheated crystal. In this region it was easier to nucleate the transition to the bcc phase than it was for melting, even though the melt was the stable phase. Even at 4 GPa, well away from the stable α phase, melting and freezing proceeded via a bcc intermediate. One is reminded of the

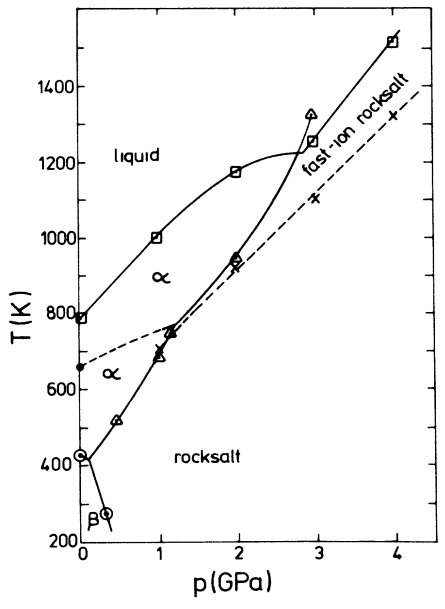

FIG. 6. The phase diagram for simulated AgI using the interaction equation (22). The triangle in the liquid phase is the rocksalt to α transition point in rocksalt-AgI superheated above the melting point. The solid data point in the α phase marks an anomaly characterized by a sharp rise in heat capacity, a rise in diffusivity and a small tetragonal distortion.

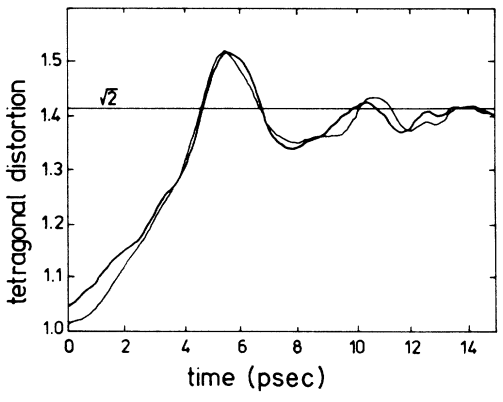

FIG. 8. The tetragonal distortion B_{22}/B_{11} and B_{33}/B_{11} during transformation from rocksalt to α-AgI at $P=0.5$ GPa and $T=589$ K.

work of Alexander and McTague[25] which uses a Landau expansion to argue for the universal preference of freezing to bcc crystal structure.

The feature of greatest interest is the course of the rocksalt–α-phase boundary which appears to confirm earlier predictions.[4] A low-angle glancing view along the data points reveals that the construction of the cusped curve is reasonable. The construction is also borne out by gradients dT_t/dp determined from the Clausius-Clapeyron equation.

Figures 9–12 show enthalpy and volume as a function of temperature for the isobars 4, 3, 2, and 0 GPa, respectively, in the 216-ion system. Each data point is obtained from equilibrations of between 2000 and 2500 cycles, i.e., for time durations of the order of 20 to 25 psec. The vertical lines in the figures denote the transition temperatures as determined using method (iii) and the various phases are annotated on the figures. Entropy changes associated with the various transitions are listed in Table I. Unfortunately, truncation of the interaction potential at the radius of the largest inscribed sphere results in a $2^{-1/2}$ reduction in truncation length on traversing the rocksalt–α-phase boundary. The distortion is manifested as an increment in enthalpy which can of course be monitored during the transition which otherwise should be isenthalpic. In Table I the entropies have been corrected for the change in truncation length, a correction which amounts to about 50% of the total entropy change.

Method (ii), that of monitoring temperature increments during adiabatic traverses of phase boundaries to obtain transition entropies, is illustrated as follows. An adiabatic run commencing at 4 GPa, 870 K, transformed at $p_3=0.5$ GPa with initial and final temperatures of $T_3=645$ K and $T_4=578$ K. p_0, T_0 is seen in Fig. 6 to be 0.7 GPa, 585 K. From the 1 GPa isobar we find

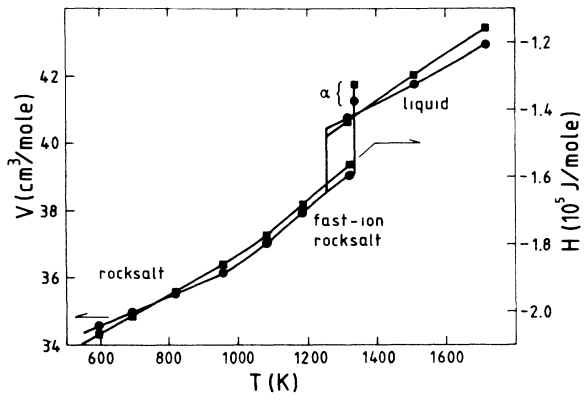

FIG. 10. Enthalpy and volume along the 3-GPa isobar.

$C_p=6.8R$ (where R is the gas constant) and using Eq. (29) as an approximation to Eq. (28) obtain

$$\Delta S_t \sim (67/585)6.8R = 0.78R \ ,$$

in good agreement with the transition entropy given in Table I at 1 GPa. In the absence of enthalpy data which yielded the above value of C_p we could still use

$$C_p \equiv C_v + \alpha(\alpha\beta_T)VT \ . \tag{30}$$

Assuming $C_v=6R$ we obtain $C_p=6.96R$ and the transition entropy is much the same as indicated above. This method could be useful for obtaining transition entropies in real experiments in the absence of calorimetric equipment.

The data in Fig. 12 for the zero-pressure isobar is interesting in that while the low-temperature equilibrations

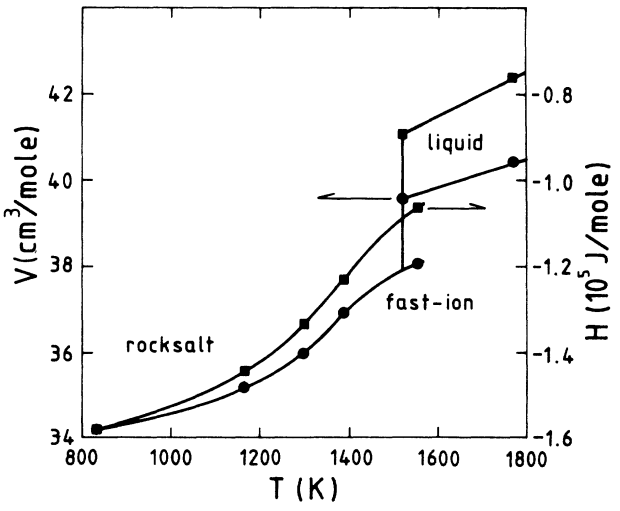

FIG. 9. Enthalpy and molar volume for simulated AgI along the 4-GPa isobar. The vertical line denotes the equilibrium melting point.

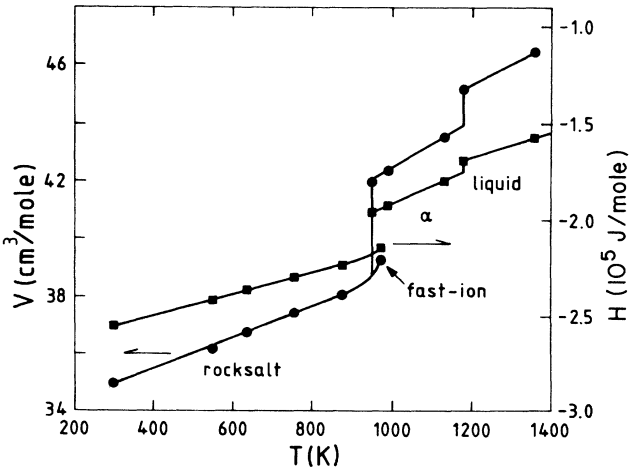

FIG. 11. Enthalpy and volume along the 2-GPa isobar. The first vertical line denotes the equilibrium rocksalt to α transition point.

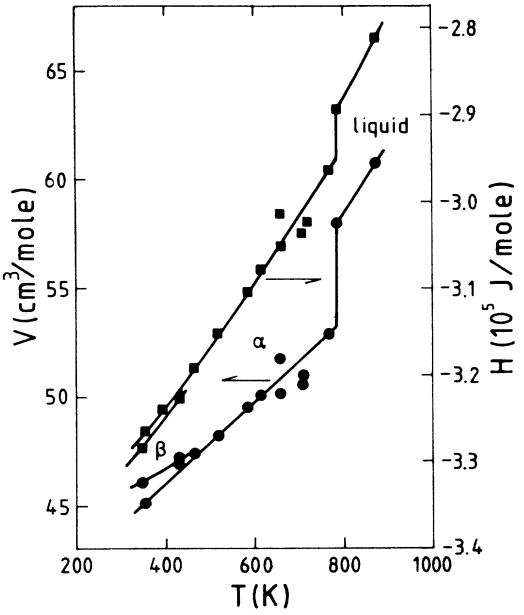

FIG. 12. Enthalpy and volume along the zero-pressure isobar. Between 650 and 700 K in the α phase the data fluctuate due to an anomaly characterized by rising heat capacity and enhanced silver-ion diffusivity.

were quite stable over the time scale employed, the results between 650 and 700 K were subject to substantial fluctuations. In view of the proposed existence of an order-disorder transition in this region and the apparent cusp in the rocksalt–α-phase boundary, this warranted further investigations. Conventional constant volume MD calculations were performed on the 51 cm^3/mole isochore to check that this is not an artifact of the constant stress algorithm. Monitoring temperature and pressure as a function of time elapsed on a constant heating rate run revealed an endotherm in the vicinity of 650 K. A sequence of configurations taken from along this heating run were equilibrated for 2000 cycles then averaged for the following 1600 to 2000 cycles and the results are presented in Fig. 13. A sigmoidal rise in internal energy and pressure is evidenced at about 630 K. The constant volume heat capacity measured from the slope of the temperature dependence of the internal energy is also shown in Fig. 13. Below the anomaly this takes the value $6.9R$, rather higher than the classical value $6R$, then rises to a maximum of $8.1R$ and falls to $6.1R$ above the anomaly. This is qualitatively the same as observed by Perrott and Fletcher[6] for real AgI where the heat capacity fell to the classical value above the anomaly.

The position of the heat-capacity maximum is indicated on our calculated phase diagram in Fig. 6 by the solid data point and its location compares remarkably favorably with the order-disorder transition of Perrot and Fletcher at 700 K. The dashed extension of this data point in the (p,T) plane shown in the figure is conjectural but it presumably extends to the cusp in the rocksalt–α-phase boundary. The breakpoints in the 0- and 1-GPa sets of diffusion data in Fig. 4 coincide with this dashed curve. It does, therefore, seem apparent that a phase anomaly occurs in the simulated α-AgI which is related to the order-disorder transition observed by Perrott and Fletcher.[6] The slopes of all three phase lines converging at the triple point have been drawn in Fig. 6 so as to satisfy the phase rule for triple points, namely,

$$\tan\gamma_{\mathrm{I}}^{\mathrm{III}}=(\Delta S_{\mathrm{I}}^{\mathrm{II}}\tan\gamma_{\mathrm{I}}^{\mathrm{II}}+\Delta S_{\mathrm{II}}^{\mathrm{III}}\tan\gamma_{\mathrm{II}}^{\mathrm{III}})/(\Delta S_{\mathrm{I}}^{\mathrm{II}}+\Delta S_{\mathrm{II}}^{\mathrm{III}})\ . \tag{31}$$

Here γ refers to the angle of slope of a phase line and the subscript and superscript roman numerals refer to initial and final phases, respectively. Though we have not shown the anomaly to be a first-order phase transition we have estimated $\Delta S_{\alpha\alpha'}$, from the heat-capacity curve in Fig. 13 to be $\Delta S_{\alpha\alpha'}=0.33R$.

TABLE I. Transition entropies $\Delta S/R$ for simulated AgI. Experimental data are shown in parentheses. The experimental value for ΔS at 1 GPa was not available, nor would it be useful for comparison. Rather, we have tabulated the experimental value at 0.6 GPa lying, at a point comparable to the simulated system at 1 GPa, just below the rocksalt fast-ion transition.

P (GPa)	$\beta\rightarrow\alpha$	fcc$\rightarrow\alpha$	$\alpha\rightarrow$melt	fcc$\rightarrow$melt
0	1.61±.06 (1.74)[a]		1.03±.03 (1.36)[b]	
1		0.79±.12 (0.78)[a]	0.74±.04	
2		1.14±.09	0.63±.05	
3		1.1±.2		1.34±.05
4				1.54±.04

[a]Reference 25.
[b]Reference 2.

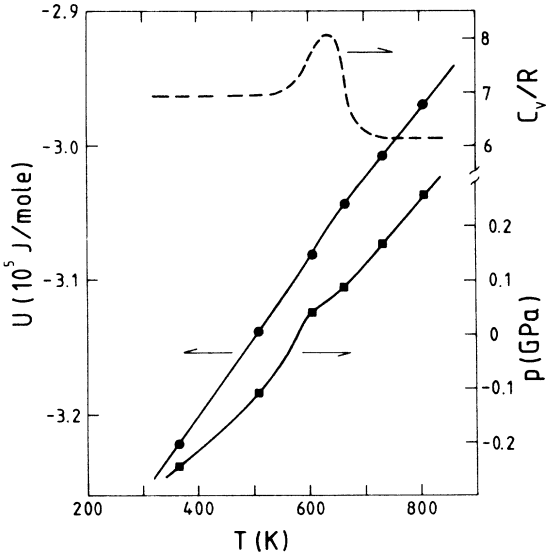

FIG. 13. Internal energy and pressure in α-AgI at a molar volume of 51 cm^3/mole using conventional constant volume MD calculations. The dashed line shows the constant volume heat capacity.

V. DISCUSSION

The above results remarkably confirm the efficacy of the Parrinello-Rahman Lagrangian in simulating changes of phase, particularly solid-solid transitions which are accompanied by shear strain. All the known regions of the phase diagram for real silver iodide are reproduced with this technique by the simple rigid-ion central potential given in Eq. (22). The scale of the investigation had placed constraints on the degree to which detail could be thoroughly explored and clearly some of the more important results remain somewhat tentative. These will of course be the subject of further study.

Two important limitations in the procedure adopted in this work give some cause for circumspection. The first is that while the various transitions were observed proceeding in both directions, the rocksalt-to-α transition and melting were only investigated in careful detail in one direction only, that of rising temperature. It is possible therefore that these transition temperatures are overestimated, particularly at higher pressures. However, the relative features, such as the cusp in the rocksalt–α-phase boundary, still stand though they may be displaced in a larger system. Moreover the diffuse fast-ion transition in the rocksalt phase is not at risk since it has no nucleation barrier. The second limitation is that, apart from the transition entropies quoted in Table I, cutoff corrections to energy and pressure have not been made. Were we to be performing conventional constant volume simulations this would be no problem, but where shape and hence cutoff radius alter substantially in a solid-solid transition the relative enthalpies of the two phases are modified and hence the phase boundary is spuriously displaced. Again, this will affect the entire phase boundary in continuous fashion so that the overall shape of the phase diagram (and the cusped boundary) still is valid. We found that simple energy and pressure corrections using the virial expression and assuming structureless far-field behavior [$g_{\alpha\beta}(r)=1,\ r>R_c$] was inadequate to represent the crystalline corrections. It may be necessary to extend interactions to the next-nearest image and maintain a constant cutoff radius to cope with this problem. We note that this difficulty is barely significant along the melting boundary as the linear expansion ranges from only 1.5% at 5 GPa to 3% at zero pressure. Moreover, the enlarged cutoff sphere probably encloses much the same number of ions as the smaller did before melting. On the other hand, with 41% changes in R_c the solid-solid transitions must be affected by cutoff corrections. Nevertheless, it is encouraging to note that the rocksalt–α-phase boundary cuts the melting line very close to the cusp at 2.8 GPa which suggests that the corrections are not very large.

While the systematic errors in the phase diagram may be quite large (though preserving all the general qualitative features shown in Fig. 6) the random errors are quite small. Much longer equilibration runs produced barely significant improvement in precision of the points of state, while the random errors in the phase boundaries are of the order of 20 to 30 K, i.e., about the height of the data points.

It is interesting to note that the supercooled α phase has a diffuse fast-ion transition shown by the plunging arrows in Fig. 4. This might be explored in real AgI by stabilizing the α phase by preparing microcrystallites, investigating thin films or by depositing AgI in a microporous medium such as zeloites. It may be, however, that, under such conditions, the rocksalt phase becomes the stable one.

The α-phase diffusion coefficients shown in Fig. 4 convincingly fall into separate low and high temperature regimes. We feel justified in the present construction rather than that of a single Ahrrenius line through all of the data for the following reasons. (i) the three sets of high-temperature data are consistent. (ii) Mellander[3] found that the activation enthalpy for silver-ion diffusion in α-AgI was independent of pressure. The present construction recognizes this, whereas single linear fits for each isobar yield a strongly pressure-dependent activation enthalpy with $h_m=0.087\pm0.007$ eV at 0 GPa and $h_m=0.132\pm0.007$ eV at 1 GPa. (iii) the breakpoints in the two curves coincide with the tentative order-disorder transition which we have shown by the dashed curve in Fig. 6. Finally, (iv) Josefson, *et al.*[27] find similar high- and low-temperature regimes in Ag^+ and Na^+ diffusion in α-AgI with activation enthalpies of (0.14 eV, 0.08 eV) and (0.17 eV, 0.09 eV), respectively. While they reported a drop in activation enthalpy from conductivity at high temperature, their plots were of $\log_{10}\sigma$ versus $10^3/T$. Mellander[3] found on replotting their data as $\log_{10}T$ versus $10^3/T$ that the activation enthalpy for ionic conductivity did indeed rise at high temperature.

Contrasting this, in their own experiments, neither Jost[7] nor Mellander[3] found any rise in activation enthalpy as indicated in Fig. 6. The conductivity data progressed free of anomaly from the β-phase boundary to the melting point. But then Mellander's samples showed no heat capacity anomaly either. We must assume that, as Perrott and Fletcher[6] found that the anomaly was suppressed by compromising stoichiometry, the samples of Mellander must have been inadequately pure or stoichiometric. Another interpretation that does not question the quality of anyone's sample is that crystallite or grain size may be significant in suppressing the effect.

The nature of the anomaly is unclear. Evidently one must investigate ionic density distribution, site occupation, hopping paths, etc., in order to clarify the behavior. Associated with the anomaly we did find a spontaneous small tetragonal distortion of the order of 5%. Even in the constant volume simulation along the 51 cm^3/mole isochore the diagonal elements of the stress tensor became unequal in the vicinity of the anomaly. This may be due to occupation of alternative equivalent tetrahedral sites. In a system as small as 216 ions there would be insufficient defective sites for the diagonal components, time averaged over only 20 to 40 psec, to equalize.

To say that further work is necessary is perhaps a little disparaging of the above results. Rather let us say that encouraged by these results we intend to pursue many of these ideas both by computer simulations and by experimentation using calorimetry and impedance spectroscopy at elevated pressures. The course of the rocksalt–α-

phase boundary is being studied using an internally heated piston-cylinder apparatus.

ACKNOWLEDGMENTS

Thanks are due to Dr. M. J. Gillan with whom the details of the constant stress MD technique, particularly as applied to Coulomb systems, were discussed and developed. The author is grateful to Theoretical Physics Division, Atomic Energy Research Establishment–Harwell, and the Department of Theoretical Physics, University of Oxford for hospitality. Funding by the Department of Scientific and Industrial Research (DSIR) is also gratefully acknowledged.

[1]B.-E. Mellander, J. E. Bowling, and B. Baranowski, Phys. Scr. **22**, 541 (1980).
[2]J. Akella, S. N. Vaidya, and G. C. Kennedy, J. Appl. Phys. **40**, 2800 (1969).
[3]B.-E. Mellander, Phys. Rev. B **26**, 5886 (1982).
[4]J. L. Tallon and R. G. Buckley, Solid State Commun. **47**, 563 (1983).
[5]M. J. Gillan and M. Dixon, J. Phys. C **13**, 1901 (1980).
[6]C. M. Perrott and N. H. Fletcher, J. Chem. Phys. **48**, 2681 (1968); **50**, 2770 (1969); **52**, 3368 (1970).
[7]W. Jost, J. Chem. Phys. **55**, 4680 (1971).
[8]P. Allen and D. Lazarus, Phys. Rev. B **17**, 1913 (1978).
[9]B. Jansson and C.-A. Sjöblom, Z. Naturforsch. **28a**, 1539 (1973).
[10]B. Jansson and C.-A. Sjöblom, Rheol. Acta **16**, 628 (1977); **20**, 360 (1981).
[11]A. Fontana, G. Mariotto, and M. P. Fontana, Phys. Rev. B **21**, 1102 (1980).
[12]Gy. Szabó, J. Phys. C **19**, L273 (1986).
[13]M. Parrinello, A. Rahman, and P. Vashishta, Phys. Rev. Lett. **50**, 1073 (1983).
[14]J. L. Tallon, Rev. Lett. **57**, 2427 (1986).
[15]H. C. Andersen, J. Chem. Phys. **72**, 2384 (1980).
[16]M. Parrinello and A. Rahman, Phys. Rev. Lett. **45**, 1196 (1980).
[17]M. Parrinello, in Computer Simulation in Physical Metallurgy, European Economic Community ISPRA Course, 1984 (unpublished).
[18]L. Verlet, Phys. Rev. **159**, 98 (1967).
[19]P. Ewald, Ann. Phys. (N.Y.) **64**, 253 (1921).
[20]A. Rahman and P. Vashista, *Physics of Superionic Conductors and Electrode Materials,* edited by J. W. Perram, NATO Advanced Study Institute (Plenum, New York, 1983) p. 93.
[21]M. J. L. Sangster and M. Dixon, Adv. Phys. **25**, 247 (1976).
[22]G. L. Chiarotti, G. Jacucci, and A. Rahman, Phys. Rev. Lett. **57**, 2395 (1986).
[23]J. L. Tallon, Aust. J. Phys. **38**, 209 (1985).
[24]D. Turnbull, in *Solid State Physics,* edited by F. Seitz and D. Turnbull (Academic, New York, 1956), Vol. 3, p. 225.
[25]S. Alexander and J. P. McTague, Phys. Rev. Lett. **41**, 702 (1978).
[26]B.-E. Mellander, B. Baranowski, and A. Lundén, Phys. Rev. B **23**, 3770 (1981).
[27]A.-M. Josefson, A. Kvist, and R. Tärneberg, in *Atom Transport in Solids and Liquids,* edited by A. Lodding and T. Lagerwall (Verlag Z. für Naturforschung, Tübingen, 1971), p. 291.